PAPER

Check for updates

The structural evolution of Mo_2C and Mo_2C/SiO_2 under dry reforming of methane conditions: morphology and support effects†

Alexey Kurlov, [iD] ‡[a] Dragos Stoian, [iD][b] Ali Baghizadeh, [iD][c] Evgenia Kountoupi, [iD][a] Evgeniya B. Deeva,[a] Marc Willinger, [iD] §[c] Paula M. Abdala, [iD] *[a] Alexey Fedorov [iD] *[a] and Christoph R. Müller [iD] *[a]

The thermal carburization of MoO_3 nanobelts (nb) and SiO_2-supported MoO_3 nanosheets under a 1:4 mixture of CH_4:H_2 yields Mo_2C-nb and Mo_2C/SiO_2. Following this process by *in situ* Mo K-edge X-ray absorption spectroscopy (XAS) reveals different carburization pathways for unsupported and supported MoO_3. In particular, the carburization of α-MoO_3-nb proceeds *via* MoO_2, and that of MoO_3/SiO_2 *via* the formation of highly dispersed MoO_x species. Both Mo_2C-nb and Mo_2C/SiO_2 catalyze the dry reforming of methane (DRM, 800 °C, 8 bar) but their catalytic stability differs. Mo_2C-nb shows a stable performance when using a CH_4-rich feed (CH_4:CO_2 = 4:2), however deactivation due to the formation of MoO_2 occurs for higher CO_2 concentrations (CH_4:CO_2 = 4:3). In contrast, Mo_2C/SiO_2 is notably more stable than Mo_2C-nb under the CH_4:CO_2 = 4:3 feed. The influence of the morphology of Mo_2C and its dispersion on silica on the structural evolution of the catalysts under DRM is further studied by *in situ* Mo K-edge XAS. It is found that Mo_2C/SiO_2 features a higher resistance to oxidation under DRM than the highly crystalline unsupported Mo_2C-nb and this correlates with an improved catalytic stability. Lastly, the oxidation of Mo in both Mo_2C-nb and Mo_2C/SiO_2 under DRM conditions in the *in situ* XAS experiments leads to an increased activity of the competing reverse water gas shift reaction.

Introduction

The dry reforming of methane (DRM, eqn (1)) is a promising technology to convert two main greenhouse gases, CH_4 and CO_2, into syngas (CO and H_2), which can be further transformed into fuels or other higher value-added chemicals.[1] However, the DRM reaction is highly endothermic and thus requires high operating temperatures to reach high conversions (typically around 800 °C), making the reaction conditions very challenging with regards to catalytic stability. In particular, catalysts based on transition metals (Ru, Rh, Pt, and Ni) typically deactivate in these harsh conditions *via*

[a] Department of Mechanical and Process Engineering, ETH Zürich, Leonhardstrasse 21, CH 8092 Zürich, Switzerland. E-mail: abdalap@ethz.ch, fedoroal@ethz.ch, muelchri@ethz.ch

[b] Swiss-Norwegian Beamlines at the European Synchrotron Radiation Facility, 71 Avenue des Martyrs, Grenoble, France

[c] Scientific Center for Optical and Electron Microscopy, ETH Zürich, Auguste-Piccard-Hof 1, CH 8093 Zürich, Switzerland

† Electronic supplementary information (ESI) available. See DOI: https://doi.org/10.1039/d2cy00729k

‡ Current address: Laboratory for Bioenergy and Catalysis, Paul Scherrer Institute (PSI), 5232 Villigen PSI, Switzerland.

§ Current address: Department of Chemistry, Technical University Munich, Lichtenbergstrasse 4, 85748 Garching, Munich, Germany.

sintering and/or coke deposition due to CH_4 decomposition (eqn (2)).[2] Moreover, the reverse water gas shift reaction (RWGS, eqn (3)) competes with the DRM reaction resulting in the consumption of hydrogen and decreasing in turn the H_2:CO ratio below one. Thus, intensive research efforts are devoted to develop catalysts for the DRM with improved stability.[3–6]

$$CH_4 + CO_2 \rightleftharpoons 2CO + 2H_2 \quad \Delta H_{298K} = +247 \text{ kJ mol}^{-1} \quad (1)$$

$$CH_4 \rightarrow C + 2H_2 \quad \Delta H_{298K} = +75 \text{ kJ mol}^{-1} \quad (2)$$

$$CO_2 + H_2 \rightleftharpoons CO + H_2O \quad \Delta H_{298K} = +41 \text{ kJ mol}^{-1} \quad (3)$$
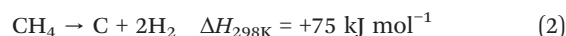
An alternative class of DRM catalysts relies on early transition metal carbides (TMC).[7,8] For instance, catalysts based on molybdenum carbide (Mo_2C) are active in DRM.[7,9–13] Advantages of carbide-based catalysts include high resistance to coking or sulfur poisoning as well as sintering resistance,[14,15] however, the high oxophilicity of early TMCs is a limitation as it often results in the deactivation of TMC-based catalysts under oxidizing atmospheres (CO_2) at high temperatures *via* the formation of oxide phases. More specifically, depending on the operating conditions, (the total pressure, the partial pressure of CO_2, temperature and the

5620 | *Catal. Sci. Technol.*, 2022, **12**, 5620–5628

This journal is © The Royal Society of Chemistry 2022

space velocity) bulk β-Mo_2C DRM catalysts can be oxidized to MoO_2 which has been linked to their deactivation.[7,16] In addition, the partial oxidation of Mo_2C to an oxycarbide phase MoC_yO_y can trigger the competing RWGS reaction.[11,17]

Approaches to yield nanostructured Mo_2C dispersed on a support can result in catalysts with an improved performance relative to the unsupported bulk carbides.[17–19] Mo_2C-based catalysts are typically obtained by the carburization of a molybdenum oxide precursor such as MoO_3 (supported or unsupported).[7,20–22] The structure and morphology of the pre-catalyst may influence the carburization pathways, the structure of the activated catalyst, its stability under DRM conditions and, thus, its performance.[7,11,16–18] The further rational development of Mo_2C-based catalysts requires an understanding of their activation and deactivation routes, i.e., understanding of the structural evolution under pre-treatment and operating conditions.[11]

In this work, using Mo K-edge X-ray absorption spectroscopy (XAS) we compare the carburization pathways of unsupported α-MoO_3 nanobelts (α-MoO_3-nb) to that of silica-supported delaminated nanosheets of MoO_3 to yield, respectively, β-Mo_2C-nb and Mo_2C/SiO_2. We further study the structural evolution of the prepared TMC-based materials under DRM conditions. By following the local structure and the oxidation state of Mo during carburization and DRM conditions by in situ Mo K-edge XAS, assisted with a multivariate curve resolution – alternating least squares (MCR-ALS) method, we reveal a difference in the carburization pathways of unsupported α-MoO_3-nb and silica supported MoO_3/SiO_2. In particular, while α-MoO_3-nb carburizes to Mo_2C-nb via intermediate (bulk) oxide phases, the carburization of MoO_3/SiO_2 proceeds via the formation of a MoO_x phase highly dispersed onto SiO_2. Although both catalysts undergo oxidation under DRM conditions leading to deactivation, we elucidate how the dispersion of Mo_2C onto SiO_2 increases its stability under DRM conditions.

Experimental

Materials

Orthorhombic α-MoO_3 nanobelts (α-MoO_3-nb) were synthesized by a reported hydrothermal method using ammonium heptamolybdate tetrahydrate (AHM, Sigma-Aldrich, 99.98% trace metals basis) and nitric acid (70%, Sigma-Aldrich, ACS reagent grade).[23] The pH of a solution of AHM (1 g) in deionized (DI) water (20 mL) was adjusted to 1 by the dropwise addition of HNO_3 (ca. 5 mL). Next, the reaction mixture was kept at 180 °C for 24 h in a Teflon-lined autoclave (45 mL). The obtained material was washed with DI water until a pH of ca. 7 was reached and subsequently dried at 100 °C.

Delaminated MoO_3 nanosheets, d-MoO_3, were obtained by the exfoliation of the synthesized α-MoO_3 according to a reported method.[24] α-MoO_3 (1 g) was ground in an agate mortar with acetonitrile (0.2 mL, Sigma-Aldrich, ACS reagent

grade, ≥99.5% purity) and the resulting material was dispersed by sonication in 50% aqueous ethanol (15 mL) for 2 h. After sonication, the suspension was centrifuged (8000 rpm, 30 min) and the supernatant containing dispersed d-MoO_3 nanosheets was collected and used for impregnation onto a SiO_2 support (150–300 μm particle size fraction of Aerosil 300 that had been calcined at 950 °C, 194 m^2 g^{-1} surface area by nitrogen physisorption).

MoO_3/SiO_2 was obtained via incipient wetness impregnation (IWI) of the supernatant solution of d-MoO_3 (ca. 1.5 mg mL^{-1} determined by thermogravimetric analysis) onto the SiO_2 support. Mo_2C-nb and Mo_2C/SiO_2 were obtained by the carburization of α-MoO_3-nb and MoO_3/SiO_2, respectively, using a mixture of H_2 and CH_4 (H_2:CH_4 = 4:1, heating at a rate of 5 °C min^{-1} from room temperature to 300 °C and from 300 °C to 800 °C at a rate of 2 °C min^{-1}, 1 h), as presented in Fig. 1a.

Characterization

Ex situ X-ray powder diffraction (XRD) data were collected using a PANalytical Empyrean X-ray diffractometer equipped with a Bragg–Brentano HD mirror and operated at 45 kV and 40 mA using $CuK_α$ radiation (λ = 1.5418 Å). The materials were examined within the 2θ range of 5–90° using a step size of 0.0167°. The scan time per step was 1 s. Thermogravimetric analysis (TGA) experiments were performed in a Mettler Toledo TGA/DSC 3 instrument. Typically, 750 μL of a colloidal solution of d-MoO_3 was placed in a sapphire crucible (900 μL) that was heated to 80 °C (5 °C min^{-1}) and kept for 1 h. Scanning electron microscopy (SEM) was performed on a Zeiss LEO Gemini 1530 microscope. All electron microscopy images were taken at an acceleration voltage of 5 kV. Prior to imaging the materials were coated with a ca. 2 nm conductive layer of platinum.

Transmission electron microscopy (TEM) was performed with a double C_S corrected JEOL JEM-ARM 300 kV TEM/STEM microscope equipped with two energy-dispersive X-ray spectroscopy (EDX) detectors with a total solid angle of 1.6 sr. The samples for TEM analysis were prepared by embedding nanobelts in the microscopy resin, sandwiched between two dummy silicon wafers, followed by tripod mechanical polishing and gentle Ar ion milling with a GATAN Precision Ion Polishing System (PIPS II) down to electron transparency. Most images were post-processed using HREM-Filters Pro, a commercially available plug-in for Digital Micrograph Package by applying Wiener filter, to reduce noise and background contributions.

In situ XAS experiments were performed at the Swiss-Norwegian Beamlines (SNBL, BM31) at the European Synchrotron Radiation Facility (ESRF, Grenoble, France). XAS spectra were collected at the Mo K-edge using a double-crystal Si (111) monochromator with continuous scanning in transmission mode. The in situ carburization followed by dry reforming of methane (DRM) experiment was performed in a quartz capillary reactor.[11,17,25] Energy calibration of the XAS
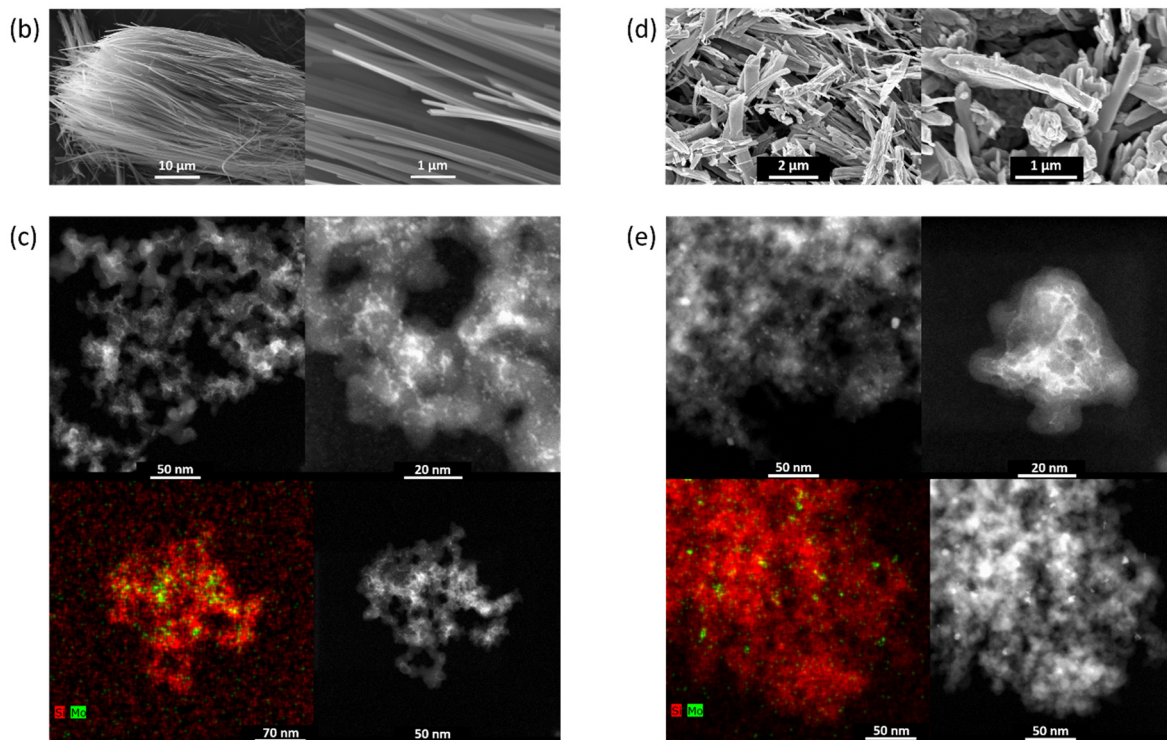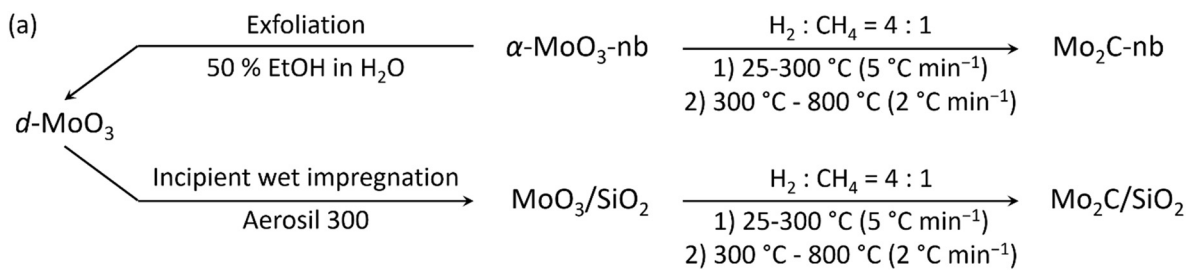
Fig. 1 a) Synthesis of Mo_2C-nb from α-MoO_3-nb and Mo_2C/SiO_2 from silica-supported delaminated MoO_3 films MoO_3/SiO_2; b) SEM images of as synthesized α-MoO_3-nb; c) HAADF-STEM images and EDX elemental (Si and Mo) maps of MoO_3/SiO_2; d) SEM images of Mo_2C-nb; and e) HAADF-STEM images and EDX maps of Mo_2C/SiO_2.

data was based on Mo foil, set at 20 000.0 eV. XAS spectra were collected in the range of 19 800.0–20 800.0 eV, with a total acquisition time of 60 s and a step of 1 eV. In the *in situ* XAS experiments, *ca.* 2 mg of the sample was placed between two quartz wool plugs in the capillary reactor (outer diameter 1.5 mm, wall thickness 0.1 mm). The carburization step was performed in a mixture of $H_2 : CH_4 = 4 : 1$ in the temperature range from 50 to 750 °C (5 mL min^{-1}, *ca.* 9 °C min^{-1} at 50–400 °C and 2 °C min^{-1} at 400–750 °C) at atmospheric pressure. DRM tests were performed at 8 bar ($CH_4 : CO_2$ He = 4 : 3 : 3) at 730 °C with the total flow rate varying in the range 1.75–3.5 mL min^{-1}. All the flow rates are express at standard conditions of temperature and pressure. Catalyst weight/ volume flow rate (W/F, in ms g_{Mo} mL^{-1}) are reported in the text below based on the nominal Mo loading. After the DRM reaction, the spent catalysts were exposed to a pure stream of CO_2 or CH_4 (5 mL min^{-1}, 730 °C). The composition of the outlet gases was monitored online by a mass spectrometer

(MS). *Ex situ* XAS data were collected on pellets of reference materials (MoO_2, α-MoO_3 and Mo_2C) with an optimized amount of sample mixed with cellulose. As-carburized Mo_2C was handled in a N_2-filled glove box to prepare specimen for XAS analysis in air-tight sealed Al bag. XAS data were processed using the Athena software (Demeter 0.9.25 software package).[26] The extracted extended X-ray absorption fine structure (EXAFS) data were k^3-weighted and the Fourier transform performed in the k-range 3–10 $Å^{-1}$ for data collected during thermal treatment and 3–12 $Å^{-1}$ for that collected at room temperature. The *in situ* time resolved normalized X-ray absorption near edge structure (XANES) data were analyzed using a MCR-ALS method.[27] MCR-ALS analysis was performed with a MATLAB software package using the multivariate curve resolution toolbox.[28] Non-negative constraints were applied for both the phase concentration and spectra profiles. The MCR-ALS analysis was complemented with principal component analysis (PCA).

Catalytic testing

The laboratory DRM tests were carried out in a fixed-bed reactor (Hastelloy X, 8 mm inner diameter) at 8 bar. In a typical experiment, 75 mg of the pre-catalyst (α-MoO$_3$-nb or MoO$_3$/SiO$_2$) was placed in between two quartz wool plugs. Prior to the catalytic tests, the pre-catalyst was transformed *in situ* into Mo$_2$C/SiO$_2$ or Mo$_2$C-nb by thermal treatment in a mixture of H$_2$:CH$_4$ = 4:1 in the temperature range from RT to 800 °C (50 mL min^{-1}, 10 °C min^{-1} at 25–300 °C and 2 °C min^{-1} at 300–800 °C) at atmospheric pressure. After this pretreatment, the pressure was increased to 8 bar (N$_2$) and the DRM feed was introduced (CH$_4$:CO$_2$:N$_2$ = 4:3:3, a total flow rate was 10 mL min^{-1}, 800 °C, 8 bar). This gives W/F *ca.* 5 ms g$_{Mo}$ mL^{-1} for Mo$_2$C/SiO$_2$ and W/F *ca.* 300 ms g$_{Mo}$ mL^{-1} for Mo$_2$C-nb. The composition of the off-gas was analyzed *via* a gas chromatograph (GC, PerkinElmer Clarus 580) equipped with a thermal conductivity detector (TCD). N$_2$ was used as an internal standard and all the outlet flow rates were calculated using following equation:

$$F_{x,\text{out}} = \frac{C_{x,\text{out}} F_{\text{N2,in}}}{C_{\text{N2,out}}} \tag{4}$$

where $F_{x,\text{out}}$ is the outlet flow rate of species x; $C_{x,\text{out}}$ is the outlet gas fraction of species x, $F_{\text{N2,in}}$ is the inlet N$_2$ flow and $C_{\text{N2,out}}$ is the outlet N$_2$ fraction.

Results and discussion

Catalyst preparation and characterization

Scanning electron microscopy (SEM) analysis of α-MoO$_3$-nb confirmed a nanobelt morphology in this material. The length of the nanobelts was typically >100 μm, their width was in the range of 200 to 400 nm and their average thickness *ca.* 50 nm (Fig. 1b). To prepare delaminated d-MoO$_3$ nanosheets, α-MoO$_3$-nb were ground and sonicated in 50% aqueous ethanol. After centrifugation, the supernatant solution contained well-dispersed MoO$_3$ nanosheets according to TEM (Fig. S1†). Using thermogravimetric analysis, the concentration of d-MoO$_3$ in the colloidal solution was determined as *ca.* 1.5 mg mL^{-1}. MoO$_3$/SiO$_2$, a material with a nominal loading of 1.75 wt% MoO$_3$, was obtained by incipient wetness impregnation of the d-MoO$_3$ colloidal solution onto a SiO$_2$ support (Aerosil 300). High angle annular dark field scanning transmission electron microscopy (HAADF-STEM) imaging of MoO$_3$/SiO$_2$ revealed a relatively homogeneous distribution of Mo (light contrast) on SiO$_2$ (dark contrast, Fig. 1c). The Mo-rich phase consisted of small agglomerates *ca.* 5 nm in size. We have reported previously that impregnation of MoO$_3$ nanosheets (contained in the colloidal solution) onto carbon spheres gives agglomerates of MoO$_3$ (mostly amorphous by TEM),[11] which are however notably larger, *i.e.* tens of nanometers, than agglomerates of MoO$_3$ on SiO$_2$ observed in this work.

Carburization of α-MoO$_3$-nb in a mixture of CH$_4$ and H$_2$ (H$_2$:CH$_4$ = 4:1) yielded Mo$_2$C-nb. SEM analysis of the carburized (and passivated) material revealed that the

carburization process does not affect notably the nanobelt morphology (Fig. 1d). XRD analysis of Mo$_2$C-nb revealed the presence of a single-phase that was assigned to β-Mo$_2$C, consistent with the complete carburization of α-MoO$_3$-nb (Fig. S2†). Similarly, the carburization of MoO$_3$/SiO$_2$ led to Mo$_2$C/SiO$_2$ (*vide infra*). STEM imaging of Mo$_2$C/SiO$_2$, (after exposure of the specimen to air during sample transfer) revealed the formation of particles of *ca.* 5–10 nm in diameter (Fig. 1e).

Catalytic performance

We evaluated and compared the DRM activity of Mo$_2$C-nb and Mo$_2$C/SiO$_2$ at 800 °C and 8 bar pressure in the laboratory-scale reactor. Mo$_2$C-nb catalyst shows a stable performance in a CH$_4$-rich flow (*i.e.* CH$_4$:CO$_2$:N$_2$ = 4:2:4) and a W/F ratio of 300 ms g$_{Mo}$ mL^{-1}. A methane conversion of *ca.* 60% under these conditions suggests that methane decomposition (eqn (2)) takes place, in line with the observations of formation of coke *via* TEM analysis (*vide infra*). Additionally, the obtained H$_2$:CO ratio of *ca.* 0.9 indicates that the reverse water gas shift (RWGS), methane decomposition and DRM reactions compete under these conditions. We also observe that the catalyst deactivated with decreasing W/F (W/F = 150 ms g$_{Mo}$ mL^{-1}) or when decreasing the CH$_4$:CO$_2$ ratio (*i.e.* CH$_4$:CO$_2$:N$_2$ = 4:3:3; methane conversion of *ca.* 10%, Fig. S3†). XRD analysis of the deactivated catalyst (after 20 h TOS, Fig. S3†) revealed formation of MoO$_2$, although β-Mo$_2$C was still present in the used catalyst (Fig. S4†).

Mo$_2$C/SiO$_2$ shows a stable catalytic performance over 8 h of time on stream (TOS) under a CH$_4$-rich flow (CH$_4$:CO$_2$:N$_2$ = 4:3:3; W/F = 5.25 ms g$_{Mo}$ mL^{-1}), with a methane conversion of *ca.* 55% (Fig. S5†). However, similarly to Mo$_2$C-nb, the obtained H$_2$:CO ratio of *ca.* 0.7 indicates that the RWGS and DRM reactions compete under these conditions.

In situ XAS under carburization conditions

To gain insight into the carburization pathways and to assess the structure and the chemical state of the activated Mo phase, we followed the transformation of α-MoO$_3$-nb to Mo$_2$C-nb by *in situ* Mo K-edge XAS using a capillary cell reactor. Based on the linear dependence of the oxidation state of Mo and the edge position of Mo in K-edge XANES spectra,[29–31] a calibration curve (based on the Mo K-edge positions of Mo, MoO$_2$ and MoO$_3$ references) was used to determine the oxidation state of Mo in analyzed samples (Fig. S6†). The XANES spectrum of α-MoO$_3$-nb has identical features to the reference spectrum of α-MoO$_3$, with a distinct pre-edge feature at 20 006.5 eV, three well-defined white line features (at *ca.* 20 026.8, 20 038.7 and 20 054.3 eV) and the edge position at 20 016.4 eV, *i.e.* in line with an oxidation state of Mo^{6+}.[29] Likewise, EXAFS analysis agrees with an α-MoO$_3$ local environment (Fig. S10†). The *in situ* XANES spectra collected during the carburization treatment showed only minor changes up to 500 °C with a slight shift of the Mo K-edge energy position to 20 015.5 eV at 500 °C (Fig. 2a and
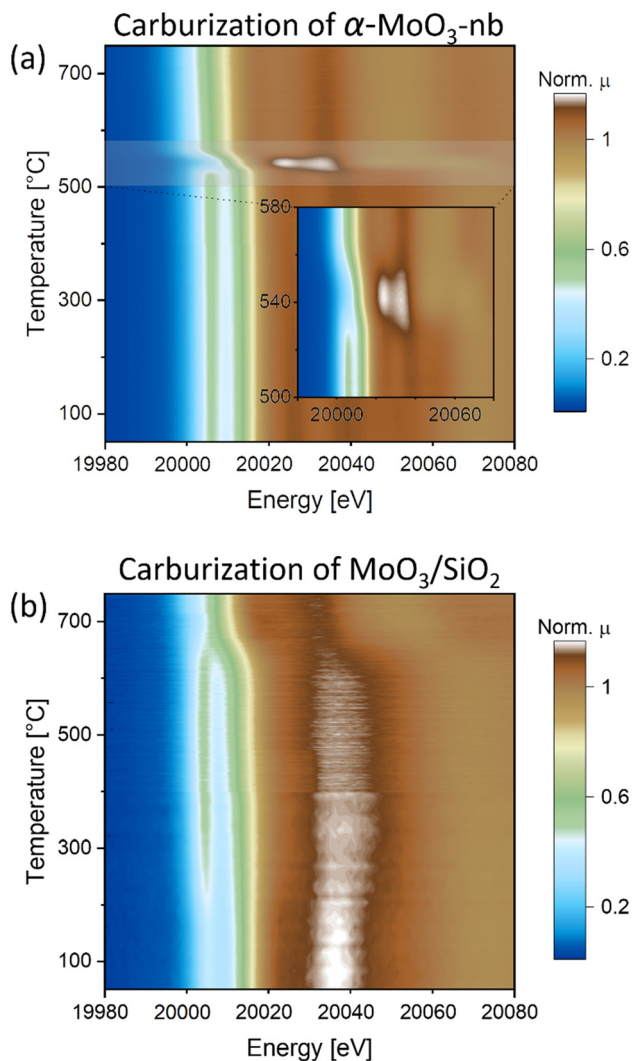
Carburization of α-MoO₃-nb

Carburization of MoO₃/SiO₂

Fig. 2 *In situ* Mo K-edge XANES (contour plots of the intensity as a function of energy and time) during carburization of a) α-MoO₃-nb and b) MoO₃/SiO₂ under $H_2 : CH_4 = 4 : 1$ gas mixture.

S7†). This shift to lower energies indicates a partial reduction of Mo, likely taking place at the surface-to-subsurface layers. The first major change occurred at *ca.* 525 °C and is manifested in the disappearance of the pre-edge feature at 20 006.5 eV and a shift of the absorption edge to 20 011.5 eV (Mo oxidation state of +4), indicating a reduction of α-MoO₃-nb to MoO_2, (see also MoO_2 reference XANES spectrum in Fig. S8†). A second transition took place at *ca.* 555 °C and is associated with a sudden shift of the Mo K-edge energy from 20 011.5 eV to 20 000.2 eV, indicating a rapid reduction of MoO_2 to Mo_2C. No further changes were observed above 750 °C and the XANES spectrum of the final phase matches the reference spectrum of β-Mo_2C, confirming the complete carburization of α-MoO₃-nb to Mo_2C-nb under the conditions applied here. The evolution of the EXAFS data agrees with the changes observed by XANES (Fig. S9†).

The XANES spectrum of MoO₃/SiO₂ showed a similar pre-edge feature (at *ca.* 20 006.5 eV) and edge energy position (at

20 016.4 eV) as the reference spectrum α-MoO₃, however it exhibited different white line features, notably with only one well-defined peak at 20 037.5 eV. We hypothesize that the different white line peaks are linked to the dispersion of MoO₃ nanosheets onto SiO₂,[32] leading to a different local structure around Mo (Fig. 2b and S7†). In line with this hypothesis, the EXAFS analysis of MoO₃/SiO₂ showed a different local structure when compared to that of α-MoO₃-nb, showing a significantly lower magnitude of the second coordination sphere pointing to a lower Mo–Mo coordination which can be linked to the high dispersion over SiO₂ (Fig. S10 and Table S1†).

Interestingly, two notable changes are observed in the *in situ* XANES spectra: one at a low temperature between 200 and 250 °C, and one at a higher temperature at *ca.* 650 °C. The low temperature transition is associated with the loss of the initially more well-defined feature around 20 037.5 eV with broadening of the white line and a more intense pre-edge feature that is also shifted to lower energies, *ca.* 20 006.2 eV (Fig. 2b and S7†). Noteworthy, the intensity of the pre-edge feature increases. The XANES spectrum of this intermediate phase does not correspond to the reference spectrum of MoO_2 and neither is it similar to the previously reported spectra of bulk Mo oxides.[31,33] However, it resembles the Mo K-edge spectra of isolated Mo-oxo species (Mo oxidation state between +5 and +6) on zeolites supports (*i.e.* ZSM-5 and H-SSZ-13).[34–36] Based on this observation, we propose that the MoO₃ phase in MoO₃/SiO₂ forms small oxo clusters and/or highly dispersed Mo oxo sites on the SiO₂ surface when the temperature reaches 200–250 °C. This is in line with the EXAFS data indicating a sudden change in the second coordination sphere at *ca.* 200 °C (Fig. S11†). The high temperature transition is associated with the disappearance of the well-defined pre-edge feature and a shift of the Mo K-edge energy from 20 015.4 eV to *ca.* 20 000.0 eV, indicating the reduction and carburization of Mo. The XANES spectrum at 750 °C corresponds to the reference spectrum of β-Mo_2C, confirming the complete carburization of MoO₃/SiO₂ to Mo_2C/SiO₂. Quantification of the phase evolution will be discussed based on MCR-ALS analysis of the XANES data (*vide infra*).

In situ XAS under DRM conditions

Next, we investigated the catalysts' structure and chemical state under DRM conditions ($CH_4 : CO_2 = 4 : 3$; at 8 bar and 730 °C) while the off-gas was analyzed by MS. Under DRM conditions, the *in situ* XANES spectra of the Mo_2C-nb catalyst (W/F = 45 ms g_{Mo} mL⁻¹) revealed an almost immediate shift of the Mo K-edge energy from 20 000.2 eV to 20 011.6 eV indicating a rapid oxidation of carbidic Mo sites in Mo_2C to a Mo^{4+} state (Fig. 3a). At the same time, a notable increase in the MS signal of H_2O was detected, indicating the presence of the competing RWGS reaction. A similar behavior under DRM conditions has been reported previously for a Mo_2C/C catalyst, *i.e.*, the oxidation of Mo to an oxycarbide phase has
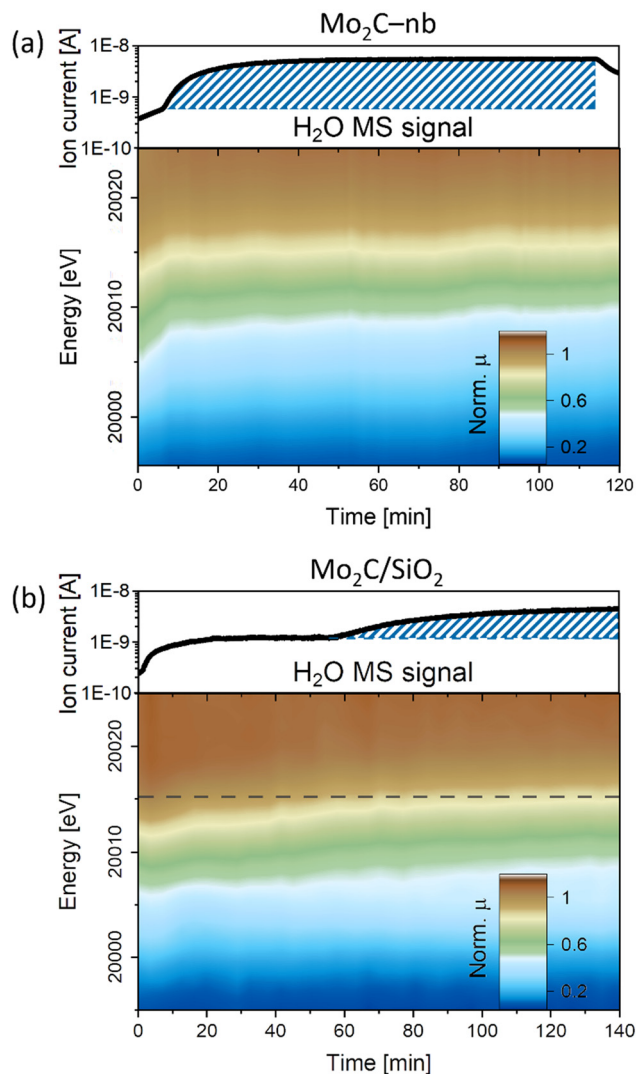
Fig. 3 *In situ* Mo K-edge XANES (contour plots of the intensity as a function of energy and time) during DRM (capillary reactor, 730 °C, 8 bar) of a) Mo_2C-nb (W/F = 45 ms g_{Mo} mL^{-1}) and b) Mo_2C/SiO_2 (W/F = 0.8 ms g_{Mo} mL^{-1}), complemented by the evolution of H_2O MS signal.

been correlated to the onset of the RWGS reaction.[11] No further significant changes were observed for the Mo_2C-nb catalyst between TOS 10 min and 120 min (Fig. 3a and S12†). Next, we exposed the deactivated Mo_2C-nb catalyst to a stream of pure CH_4 to determine if it can be regenerated. However, no changes in the XANES spectra were observed throughout the 60 min exposure of the catalyst to CH_4, indicating the irreversibility of catalyst oxidation (in these conditions).

The XANES changes during DRM of Mo_2C/SiO_2 were also evaluated (W/F = 0.8 ms g_{Mo} mL^{-1}). In contrast to the rapid oxidation of Mo_2C-nb, a slower Mo oxidation was observed for Mo_2C/SiO_2, identified by a gradual shift of the Mo K-edge to higher energies (Fig. 3b). The slower oxidation rate is consistent with the higher stability of Mo_2C/SiO_2 under DRM conditions. After *ca.* 60 min TOS, a pre-edge feature appears in the XANES spectra of this catalyst. Interestingly, consistent with the evolution of the XANES data, the MS data reveals an

increase of the H_2O signal starting from TOS = 60 min. Therefore, this indicates that the onset of the RWGS reaction coincides with a phase transformation of the catalyst (for the nature and quantitative analysis of the oxidized species *vide infra* MCR-ALS analysis).[11] Additional exposure of the catalyst to a stream of pure CO_2 shifts the Mo K-edge to higher energies, indicating a further oxidation of the material (Fig. S13†). Additionally, the intensity of the pre-edge feature increases significantly and the XANES spectrum at the end of the reaction corresponds clearly to the intermediate phase observed during carburization. Interestingly, contrary to the deactivated Mo_2C-nb catalyst, an oxidized Mo_2C/SiO_2 can be partially reduced (and likely, recarburized) under a pure stream of CH_4 (Fig. S13†). This observation indicates that a dynamic oxidation-recarburization process may in principle take place under DRM conditions,[7] yet it has been reported that addition of transition metals such as Ni is required to increase the rate of recarburization, in order to match the oxidation rate.[12,13]

Phase evolution by MCR-ALS analysis of *in situ* XAS data

A quantitative analysis of the *in situ* XANES data was performed *via* the MCR-ALS method combined with principal component analysis. This method allowed us to assess the phase evolution during carburization and DRM, as well as to extract the main components that describe the dynamics of the investigated materials. The analysis of the Mo_2C-nb system revealed that the carburization and DRM processes could be fully described using four distinct components (Fig. S14†). Those four spectra (C_1, C_2, C_3 and C_4), extracted using MCR-ALS analysis, are presented in Fig. S15.† To assign the extracted components, we compare them with available references spectra. Component C_1 is identical to that of α-MoO_3 and the spectrum of component C_4 is identical to that of β-Mo_2C. Component C_2 possess a well-defined pre-edge at *ca.* 20 007.1 eV, albeit of a lower intensity as compared to C_1. The Mo K-edge position in C_2 was determined as 20 015.8 eV revealing an estimated Mo oxidation state between +5 and +6. Based on this oxidation state and the resemblance of the spectrum to that of Mo_4O_{11},[33] we ascribe the C_2 component to Mo_4O_{11} or to a mixture of different MoO_x (*e.g.* Mo_4O_{11}, Mo_8O_{23}, $Mo_{17}O_{47}$, *etc.*) species. Lastly, the Mo K-edge position (20 011.9 eV) and the XANES features of component C_3 resembles strongly that of MoO_2, which allows us to ascribe C_3 to MoO_2. The changes of the fractions of components C_1–C_4 with increasing carburization temperature are presented in Fig. 4a. The MCR analysis indicates that C_1 (MoO_3) is stable up to *ca.* 495 °C and from 495 °C this component starts to transform rapidly to C_2 followed by C_3; it disappears completely at *ca.* 535 °C. The C_2 component was found to be very short-lived, reaching its maximum fraction of 0.64 at 530 °C while completely disappearing already at 565 °C and being replaced by a mixture of C_3 and C_4. The C_3 component (assigned to MoO_2) appears at *ca.* 525 °C and quickly reaches its maximum
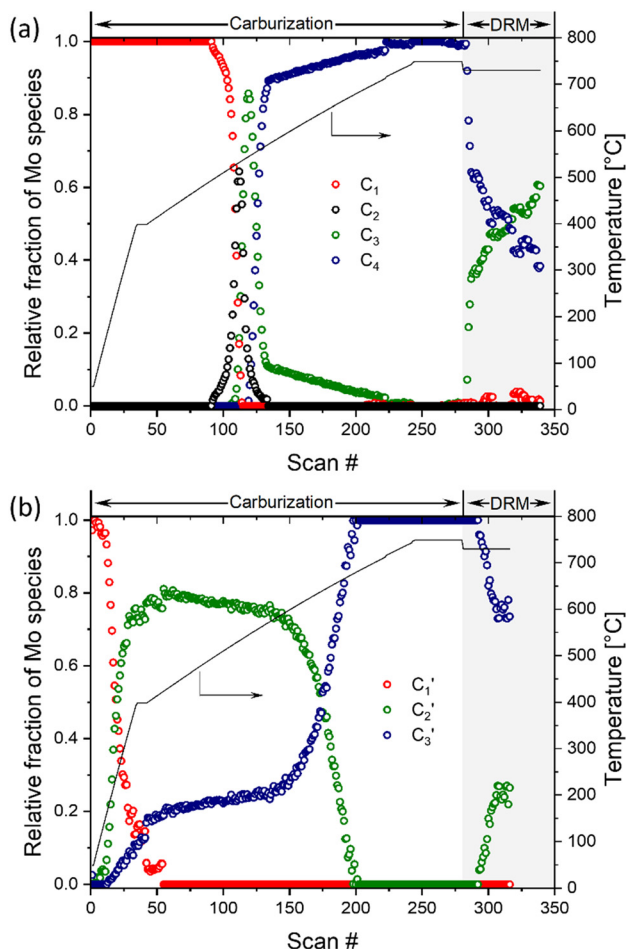
This journal is © The Royal Society of Chemistry 2022

Catal. Sci. Technol., 2022, **12**, 5620–5628 | **5625**

Fig. 4 Phase evolution of a) α-MoO$_3$-nb and b) MoO$_3$/SiO$_2$ during the carburization process and DRM according to MCR-ALS of the XANES data.

fraction of 0.85 at 545 °C. Subsequently, the concentration of C$_3$ decreases rapidly being replaced by C$_4$ (Mo$_2$C, which appears at 545 °C) and drops down to a fraction *ca.* 0.1 at 570 °C. Increasing the temperature further, yield a further decrease of the fraction of MoO$_2$ until it disappears completely at *ca.* 710 °C (Fig. 4a). This observation can be explained by the slow carburization of the core of the nanobelts.

Turning to the Mo$_2$C/SiO$_2$ catalyst, only three distinct components are involved in the carburization process (Fig. S16†). Those three spectra (C$'_1$, C$'_2$ and C$'_3$) extracted using MCR-ALS analysis are presented in Fig. S17.† Component C$'_1$ is assigned to the initial MoO$_3$ phase dispersed onto SiO$_2$ (*vide supra*). The intermediate C$'_2$ component shows a unique white line shape which resembles the Mo K-edge spectra of previously reported molybdenum single sites (MO$_x$/SiO$_2$).[34–36] The edge energy (20 015.4 eV) indicates Mo in an oxidation state between +5 and +6. Component C$'_3$ shows similar features to that of the β-Mo$_2$C reference and thus is assigned to the carburized Mo (Mo$_2$C) supported on SiO$_2$. Fig. 4b plots the changes of the fraction of the C$'_1$, C$'_2$ and C$'_3$ components during the carburization process. The intermediate C$'_2$ component

starts to appear at *ca.* 120 °C and reaches its maximum level of *ca.* 0.8 at 400 °C. The fraction of the component C$'_1$, corresponding to the initial state of the material, reduces rapidly until it disappears at *ca.* 425 °C. Interestingly, the MCR analysis indicates that the molybdenum carbide phase (C$'_3$) appears already at *ca.* 200 °C and reaches a fraction of *ca.* 0.2 at 425 °C during the initial stage of carburization. The concentration of C$'_3$ starts to increase slowly replacing C$'_2$ until it reaches a weight fraction of 0.3 at *ca.* 600 °C. Afterwards, a rapid carburization of C$'_2$ to C$'_3$ occurs yielding a pure C$'_3$ phase at *ca.* 680 °C (Fig. 4b).

The MCR analysis indicates that the changes in the XANES spectra under DRM conditions can be described with the same components that have been identified in the carburization process (Fig. 4a and b). In particular, for Mo$_2$C-nb the evolution of the *in situ* XANES data during DRM conditions can be fully described with the components MoO$_2$ (C$_3$) and Mo$_2$C (C$_4$). The MCR analysis indicates that under DRM conditions Mo$_2$C is rapidly oxidized to MoO$_2$ yielding a fraction of MoO$_2$ of >0.6 after 120 min TOS (Fig. 4a).

The evolution of the *in situ* XANES spectra of Mo$_2$C/SiO$_2$ during DRM can be fully described by the components C$'_2$ and C$'_3$ (Mo$_2$C) (Fig. 4b). However, the MCR analysis indicates no changes in the phase composition during 45 min TOS revealing that only C$'_3$ (Mo$_2$C) is present until up to 45 min under DRM conditions. Subsequently, a slow oxidation of Mo$_2$C into C$'_2$ (MO$_x$/SiO$_2$) is revealed, reaching asymptotic fractions of 0.75 for Mo$_2$C and 0.25 for C$'_3$ after *ca.* 120 min TOS (Fig. 4b). To summarize, our studies reveal that the degree of oxidation of the carbidic phase in Mo$_2$C/SiO$_2$ is lower than for Mo$_2$C-nb under DRM conditions. It should be highlighted that although in the *in situ* XANES setup requires a different W/F ratio as compared to the laboratory reactor system (*i.e.* parameters of the synchrotron experimental setup yield a *ca.* one order of magnitude lower W/F ratio as compared to the laboratory reactor), and this can affect the degree of catalysts oxidation, both laboratory reactor and synchrotron capillary experiments provide qualitatively similar results. The observed MoO$_2$ phase *via ex situ* XRD analysis of the spent catalyst (Fig. S4†) correlates well with the *in situ* XANES analysis.

It has been previously reported that the carburization of MoO$_3$/C to Mo$_2$C/C and the evolution of Mo$_2$C/C under DRM conditions involves an oxycarbide intermediate.[11] In contrast, we do not observe oxycarbide intermediates in the current study, despite similar experimental conditions and the same starting Mo precursor (d-MoO$_3$). This may be explained by the support effect, that is, the carbon support in MoO$_3$/C and Mo$_2$C/C enables carburization and DRM pathways that involve a Mo$_2$C$_x$O$_y$ intermediate that seems to be hindered for Mo$_2$C-nb and Mo$_2$C/SiO$_2$ of this work. That being said, we cannot exclude the formation of surface oxycarbides that can bring about the RWGS reactivity of *in situ* oxidized Mo$_2$C-nb and Mo$_2$C/SiO$_2$.

5626 | *Catal. Sci. Technol.*, 2022, **12**, 5620–5628

This journal is © The Royal Society of Chemistry 2022

Morphology of the used catalyst

Lastly, the morphology of the reacted Mo_2C-nb catalyst (after 20 h TOS, Fig. S3,† followed by passivation) was investigated using SEM and TEM. The SEM analysis revealed that while Mo_2C-nb$_{reacted}$ has preserved its nanobelt morphology, the initially smooth nanobelt surface is found to be decorated by small particles (Fig. S18†). To determine the nature of the observed particles Mo_2C-nb$_{reacted}$ was analyzed further using TEM. A cross-section of Mo_2C-nb$_{reacted}$ reveals that it is porous, *i.e.*, every nanobelt consists of *ca.* 10–20 nm particles (Fig. S19†). This observation can be possibly explained by the significantly lower molar volume of Mo_2C compared to MoO_3 (*i.e.* $V_m(MoO_3)$ = 30.6 cm^3 mol^{-1}, $V_m(MoO_2)$ = 19.8 cm^3 mol^{-1}, $1/2V_m(Mo_2C)$ = 11.5 cm^3 mol^{-1}) leading to the formation of voids during the carburization process. High resolution TEM imaging reveals that particles are often covered with graphitic and/or amorphous carbon (Fig. S20†), indicating methane decomposition (eqn (2)) during DRM that results in coke deposition. Since the catalyst deactivation test presented in Fig. S3† uses two ratios of $CH_4:CO_2$, *i.e.* an initial 2:1 ratio is followed by a 4:3 ratio, coking likely proceeds in the CH_4-rich feed while the catalyst oxidation (from Mo_2C to MoO_2) likely proceeds in the CO_2-rich feed; both processes lead to the catalyst deactivation (Fig. S3†). Analysis of the lattice fringes of the particles coated by coke shows that these particles are composed of Mo_2C.

Conclusions

In situ Mo K-edge XAS uncovered that unsupported MoO_3 nanobelts and MoO_3/SiO_2 undergo different carburization pathways (using a 1:4 mixture of $CH_4:H_2$) to form, respectively, Mo_2C and Mo_2C/SiO_2. The carburization of α-MoO_3-nb proceeds *via* MoO_2, and that of MoO_3/SiO_2 *via* the formation of highly dispersed MoO_x species. Catalytic tests show that both carburized materials provide a stable performance in the DRM reaction at an elevated pressure of 8 bar and a CH_4-rich flow (*i.e.* $CH_4:CO_2:N_2$ = 4:2:4). In particular, unsupported Mo_2C-nb shows a stable performance at high W/F = 300 ms g_{Mo} mL^{-1}, but deactivates when decreasing W/F (to 150 ms g_{Mo} mL^{-1}) or when increasing the CO_2 concentration. The dispersion of Mo_2C onto SiO_2 increases significantly the stability of the catalyst under DRM conditions. In particular, Mo_2C/SiO_2 exhibits a high stability over 8 h TOS at W/F = 5.25 ms g_{Mo} mL^{-1}. *In situ* XAS showed that under DRM conditions Mo_2C oxidizes to MoO_2 leading to catalytic deactivation. The degree of oxidation is different between Mo_2C-nb and Mo_2C/SiO_2, whereby Mo_2C/SiO_2 is more resistant towards oxidation under DRM conditions, *i.e.* *ca.* 75% of Mo_2C remained in Mo_2C/SiO_2 and the rest is MO_x/SiO_2 (without MoO_2 formation) after 120 min TOS as compared to only 40% of Mo_2C for Mo_2C-nb. *In situ* XAS experiments show a clear correlation between the increased activity in the undesired competing reverse water gas shift reaction and the oxidation of carbidic Mo in Mo_2C-nb and Mo_2C/SiO_2 under DRM conditions.

Author contributions

This article was prepared and written through contribution of all the authors. All authors have read and agreed to the final version of the manuscript.

Conflicts of interest

The authors declare that there is no conflict of interest regarding the publication of this article.

Acknowledgements

References

1 M. S. Fan, A. Z. Abdullah and S. Bhatia, *ChemCatChem*, 2009, **1**, 192–208.

2 D. Pakhare and J. Spivey, *Chem. Soc. Rev.*, 2014, **43**, 7813–7837.

3 L. C. Buelens, V. V. Galvita, H. Poelman, C. Detavernier and G. B. Marin, *Science*, 2016, **354**, 449–452.

4 S. M. Kim, P. M. Abdala, T. Margossian, D. Hosseini, L. Foppa, A. Armutlulu, W. van Beek, A. Comas-Vives, C. Coperet and C. Muller, *J. Am. Chem. Soc.*, 2017, **139**, 1937–1949.

5 Z. Bian and S. Kawi, *J. CO2 Util.*, 2017, **18**, 345–352.

6 M. A. Naeem, P. M. Abdala, A. Armutlulu, S. M. Kim, A. Fedorov and C. R. Müller, *ACS Catal.*, 2020, **10**, 1923–1937.

7 J. B. Claridge, A. P. E. York, A. J. Brungs, C. Marquez-Alvarez, J. Sloan, S. C. Tsang and M. L. H. Green, *J. Catal.*, 1998, **180**, 85–100.

8 Z. Lin, S. R. Denny and J. G. Chen, *J. Catal.*, 2021, **404**, 929–942.

9 A. J. Brungs, A. P. E. York, J. B. Claridge, C. Marquez-Alvarez and M. L. H. Green, *Catal. Lett.*, 2000, **70**, 117–122.

10 D. C. LaMont and W. J. Thomson, *Chem. Eng. Sci.*, 2005, **60**, 3553–3559.

11 A. Kurlov, X. Huang, E. B. Deeva, P. M. Abdala, A. Fedorov and C. R. Müller, *Nanoscale*, 2020, **12**, 13086–13094.

12 C. G. Silva, F. B. Passos and V. d. S. T. da Silva, *J. Catal.*, 2019, **375**, 507–518.

13 R. D. Barbosa, M. A. S. Baldanza, N. S. de Resende, F. B. Passos and V. L. d. S. T. da Silva, *Catal. Lett.*, 2020, **151**, 1578–1591.

14 P. Da Costa, J.-L. Lemberton, C. Potvin, J.-M. Manoli, G. Perot, M. Breysse and G. Djega-Mariadassou, *Catal. Today*, 2001, **65**, 195–200.

15 A. Mehdad, R. E. Jentoft and F. C. Jentoft, *J. Catal.*, 2017, **347**, 89–101.

16 D. C. LaMont, A. J. Gilligan, A. R. S. Darujati, A. S. Chellappa and W. J. Thomson, *Appl. Catal., A*, 2003, **255**, 239–253.

17 A. Kurlov, E. B. Deeva, P. M. Abdala, D. Lebedev, A. Tsoukalou, A. Comas-Vives, A. Fedorov and C. R. Müller, *Nat. Commun.*, 2020, **11**, 4920.

18 H. Gao, Z. Yao, Y. Shi and S. Wang, *Catal. Sci. Technol.*, 2018, **8**, 697–701.

19 A. R. S. Darujati and W. J. Thomson, *Appl. Catal., A*, 2005, **296**, 139–147.

20 C. Shi, A. Zhang, X. Li, S. Zhang, A. Zhu, Y. Ma and C. Au, *Appl. Catal., A*, 2012, **431-432**, 164–170.

21 T. Mo, J. Xu, Y. Yang and Y. Li, *Catal. Today*, 2016, **261**, 101–115.

22 M. M. Sullivan, C.-J. Chen and A. Bhan, *Catal. Sci. Technol.*, 2016, **6**, 602–616.

23 A. Chithambararaj, N. Rajeswari Yogamalar and A. C. Bose, *Cryst. Growth Des.*, 2016, **16**, 1984–1995.

24 F. Ji, X. Ren, X. Zheng, Y. Liu, L. Pang, J. Jiang and S. Liu, *Nanoscale*, 2016, **8**, 8696–8703.

25 W. van Beek, O. V. Safonova, G. Wiker and H. Emerich, *Phase Transitions*, 2011, **84**, 726–732.

26 B. Ravel and M. Newville, *J. Synchrotron Radiat.*, 2005, **12**, 537–541.

27 A. Tsoukalou, P. M. Abdala, D. Stoian, X. Huang, M. G. Willinger, A. Fedorov and C. R. Muller, *J. Am. Chem. Soc.*, 2019, **141**, 13497–13505.

28 J. Jaumot, A. de Juan and R. Tauler, *Chemom. Intell. Lab. Syst.*, 2015, **140**, 1–12.

29 S. P. Cramer, T. K. Eccles, F. W. Kutzler, K. O. Hodgson and L. E. Mortenson, *J. Am. Chem. Soc.*, 1976, **98**, 1287–1288.

30 T. Ressler, J. Wienold, R. E. Jentoft and T. Neisius, *J. Catal.*, 2002, **210**, 67–83.

31 E. B. Deeva, A. Kurlov, P. M. Abdala, D. Lebedev, S. M. Kim, C. P. Gordon, A. Tsoukalou, A. Fedorov and C. R. Müller, *Chem. Mater.*, 2019, **31**, 4505–4513.

32 Z. Huang, W. Bensch, W. Sigle, P. A. van Aken, L. Kienle, T. Vitoya, H. Modrow and T. Ressler, *J. Mater. Sci.*, 2007, **43**, 244–253.

33 T. Ressler, R. E. Jentoft, J. Wienold, M. M. Günter and O. Timpe, *J. Phys. Chem. B*, 2000, **104**, 6360–6370.

34 I. Lezcano-Gonzalez, R. Oord, M. Rovezzi, P. Glatzel, S. W. Botchway, B. M. Weckhuysen and A. M. Beale, *Angew. Chem., Int. Ed.*, 2016, **55**, 5215–5219.

35 N. Kosinov, E. A. Uslamin, L. Meng, A. Parastaev, Y. Liu and E. J. M. Hensen, *Angew. Chem., Int. Ed.*, 2019, **58**, 7068–7072.

36 M. Agote-Aran, A. B. Kroner, D. S. Wragg, W. A. Slawinski, M. Briceno, H. U. Islam, I. V. Sazanovich, M. E. Rivas, A. W. J. Smith, P. Collier, I. Lezcano-Gonzalez and A. M. Beale, *Molecules*, 2020, **25**, 5048.